Mustafa A. Najim
Mustafa A. Hassan
Khaleel I. Hassoon

Department of Applied Sciences,
University of Technology – Iraq,
Baghdad 10066, IRAQ

Well-Modified Morphology of CuO Thin Films Using NiO and Fe₂O₃ Seed Layers

In this work, nickel oxide and ferric oxide thin films prepared by chemical spray pyrolysis (CSP) were used as seed layers for the deposition of cupric oxide by chemical bath deposition (CBD). The aim was to investigate the effect of these seed layers on the structural, optical, and electrical properties of CuO prepared by CBD. XRD analysis confirmed the formation of CuO thin films on Fe_2O_3 and NiO seed layers. The FESEM analysis showed that the morphology of CuO thin films is influenced by the type of seed layer. AFM results showed that smoother surfaces led to better CuO thin films morphologies. The energy gap was obtained using an innovative method from uv-vis spectroscopy measurements. Hall's effect measurements revealed that the obtained CuO films exhibited p-type conductivity and DC-conductivity were highest in samples that exhibited highest dislocation densities.

1. Introduction

Metal oxides are inorganic materials composed of a metal cation and oxygen as an anion. They demonstrate unique and remarkable properties in their bulk or nanostructure forms. The functional properties of metal oxides are related to their features such as crystal structure, composition, existing defects, and introduced doping. Such features dictate the optical, electrical, and structural properties of the metal oxide structure [1,2]. The methods used for metal-oxide deposition and the parameters involved in the deposition play a vital role in shaping the morphology of the nanostructured metal oxides thus affecting the resultant properties [3]. The versatility of their properties makes them suitable in modern-era applications, such as, display technology [4], sensors [5,6], antistatic films [7], supercapacitors [8], biology [9,10] and optoelectronics and solar cells [11-13].

Amongst these important metal oxides is copper oxide. It exists commonly in two oxidation forms, copper (I) oxide or cuprous oxide (Cu_2O) and copper (II) oxide or cupric oxide (CuO). Both are p-type semiconductors, and they have cubic and monoclinic crystalline structures with energy gaps ranging roughly in 2.2-2.6 eV and 1.5-2.2 eV, respectively [15-17].

Another type of metal oxide is iron oxide. This oxide has been a focal point of much modern research due to its ease of deposition, availability in the earth crust, and versatility of its properties. Ferric oxides can have an amorphous phase or polycrystalline phase, their polymorphs α-Fe_2O_3, β-Fe_2O_3, γ-Fe_2O_3, and ε-Fe_2O_3 exhibit distinct structural configurations. The type of conductivity and value of the energy gap is dependent on the phase of iron oxide. The bandgap energy usually in the range of 2.0-2.8 eV [18,19]. Fe_2O_3 is generally utilized in applications related to gas sensing and magnetism [20,21].

On the other hand, nickel oxide is a transparent conductive oxide with a rock salt crystalline structure with octahedral Ni^{2+} and O^{2-} sites [22]. It has a p-type conductivity with a relatively higher energy bandgap ranging from 3.6 to 4.0 eV [23].

These oxides can be deposited using various chemical and physical deposition methods such as chemical bath deposition [16], sputtering [23], sol-gel [20,24], and chemical spray pyrolysis (CSP) [17,25]. Chemical spray pyrolysis [26] and chemical bath deposition [16] both stand out as techniques that don't require advanced lab equipment or a high level of operational expertise yet yield superb quality products while offering good control over the thickness and homogeneity of the resultant film [25].
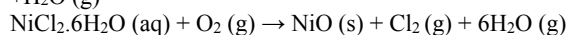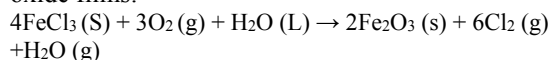
By reviewing the literature regarding metal oxide thin film deposition, it has been found that depositing a film on a seed layer affects its structural properties and thus yields properties reliant on the type of seed on which it is deposited. As is shown when depositing zinc oxide film on the seed layer, the resultant film nanorod structure had higher surface areas and more regularity when deposited on the low-thickness seed layer [27,28].

Based on the limited studies conducted on using seed layers as substrates for the deposition of CuO by chemical bath method, our study investigates the impact of NiO and Fe_2O_3 as seed layers deposited by CPS on the functional properties of cupric oxide thin films prepared by CBD.

2. Experimental Work

In this study, CSP was implemented to deposit Fe_2O_3 and NiO seed layers on microscopic slides. Two metal salt-based precursor solutions were prepared from dissolving ferric chloride $FeCl_3$ and nickel chloride hexahydrate $NiCl_2.6H_2O$ in deionized water to obtain two solutions with 0.1 M concentration. Each

solution was subjected to agitation via a magnetic stirrer for 5 minutes until we achieved a light brown color for the FeCl₃ solution and a light green color for the NiCl₂.6H₂O solution which signifies the complete dissolution of metal salts into the solvent. Glass slides were selected as substrates for the seed layers, they underwent cleaning by hydrochloric acid at 8% concentration following washing in ethanol and deionized water respectively. The precursor solutions were sprayed at 45° angle on glass substrates at a flow rate of 2 ml/min and a fixed temperature of 400°C. The process was done by implementing filtered air as carrier gas compressed to 6 kg/cm² pressure. After spraying process, the resultant seed layers were washed by ethanol and deionized water to clean any unwanted particles that may act as impurities or contribute to heterogeneous nucleation for the subsequent process. The following chemical reactions elaborate the thermal decomposition of the solution and the formation of oxide films:

$4FeCl_3 (S) + 3O_2 (g) + H_2O (L) \rightarrow 2Fe_2O_3 (s) + 6Cl_2 (g) + H_2O (g)$

$NiCl_2.6H_2O (aq) + O_2 (g) \rightarrow NiO (s) + Cl_2 (g) + 6H_2O (g)$

The CSP setup was the same as that utilized in depositing Sr-doped CuO thin films in reference [25]. Later, the CuO films were deposited on the resultant seed layers via CBD process. The precursor solution was prepared by dissolving cupric chloride dihydrate CuCl₂.2H₂O in deionized water to obtain a 0.1 M concentration of cupric chloride solution. The resultant solution temperature and pH were raised and maintained at 90°C and 10.0, respectively, by employing hotplate stirrer and ammonium hydroxide of 30% concentration as a complexing agent. The solution experienced color change, transitioning from a clear blue to deep blue, and ultimately to brownish black indicating the formation of copper (I) oxide, copper (II) oxide and copper hydroxide particles. The solution was subjected to magnetic stirrer agitation throughout the process to ensure an even distribution of heat and homogeneity of the solution. The resultant film was annealed for 2 hours at 400°C. The following chemical equation demonstrates the process of chemical bath deposition:

$CuCl_2.2H_2O (aq) \rightarrow Cu^{+2} (aq) + 2Cl^{-2} (aq)$

$NH_3 + H_2O \rightarrow NH_4^+ (aq) + OH^- (aq)$

$Cu^{+2} (aq) + 2OH^- (aq) \rightarrow Cu(OH)_2$
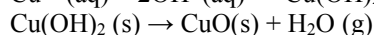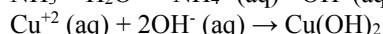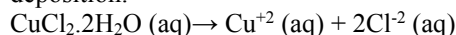
$Cu(OH)_2 (s) \rightarrow CuO(s) + H_2O (g)$

Figure (1) demonstrates the setup of the chemical bath deposition system:

The produced seed layers and thin film structural properties were characterized by a Shimadzu XRD-6000 x-ray diffractometer to determine their crystalline structure, crystallite size, and dislocation density. An Inspect f50-FEI field-emission electron microscope (FE-SEM) was used to investigate the surface morphology and to measure the average thickness via cross section imaging. An AA3000 scanning probe

atomic force microscope (AFM) was utilized to study the topography and the roughness. The optical properties of the deposited seed layers and thin films were investigated using a Metertech SP8001 400-1100nm UV-Visible spectrophotometer to determine their optical bandgap and absorption coefficient. The baseline absorption of the seed layers has been omitted by using the corresponding seed layer as a reference in the UV-visible system. Hall effect and DC conductivity tests were implemented to find the type of conductivity, charge carrier density, carrier's mobility, and conductivity as a function of temperature. Further within this article we use the following notations: FG: Fe₂O₃ on Glass, CF: CuO on Fe₂O₃, NG: NiO seed layer on Glass, CN: CuO on NiO, and CG: CuO on Glass.
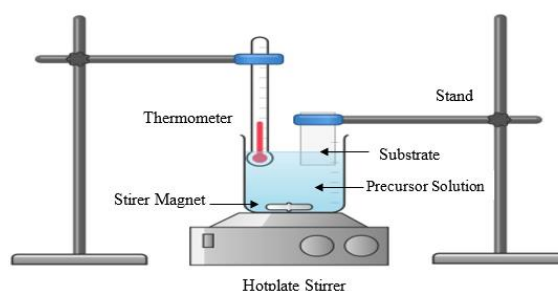

Fig. (1) Experimental setup for the CBD system

3. Results and Discussions

The XRD patterns of NiO and Fe₂O₃ seed layers along with CuO deposited by CBD on each seed layer are shown in Fig. (2). Fe₂O₃ seed layer exhibiting two peaks, one with higher intensity at 33.21° and the other with lower intensity at 35.64° corresponding to (104) and (101) planes, respectively, which agree with [29]. NiO seed layer exhibiting only one peaks at 37.27° corresponding to (111) plane indicating the existence of single crystal type, similar XRD readings obtained in reference [30]. CuO films deposited on each previously mentioned seed and CuO deposited directly on glass without the seed layer exhibited only two peaks with different intensities at 35.75° and 38.95°. The intensity of peaks is greatly affected when deposited on the NiO seed layer indicating a noticeable increase in the diffraction peak at 35.75°, mimicking the pattern of the NiO seed layer.

The average crystallite size (D) and the dislocation density (δ) were determined by Scherrer's formula (Eq. 1) [31] and Eq. (2) [32], respectively, for both the seed layers and the CuO thin films

$$D = \frac{0.9\lambda}{\beta cos\theta} \qquad (1)$$

$$\delta = \frac{1}{D^2} \qquad (2)$$

The data in table (1) indicates that CuO, NiO and Fe₂O₃ thin films deposited on glass (CG, NG and FG) have in general maximum crystallite size. Based on FE-SEM and AFM results, the reduction in crystallite size is more obvious when CuO is deposited on a rougher

seed layer in turn led to an increase in the dislocation densities (δ) as presented in table (1). On the other hand, if we look at AFM results, we conclude that the obtained microstrain values for CN and CF samples indicate that the smoother seed layers on which CuO films was deposited have less microstrain values and the sample FG which had the roughest surface is possessing largest microstrain value.
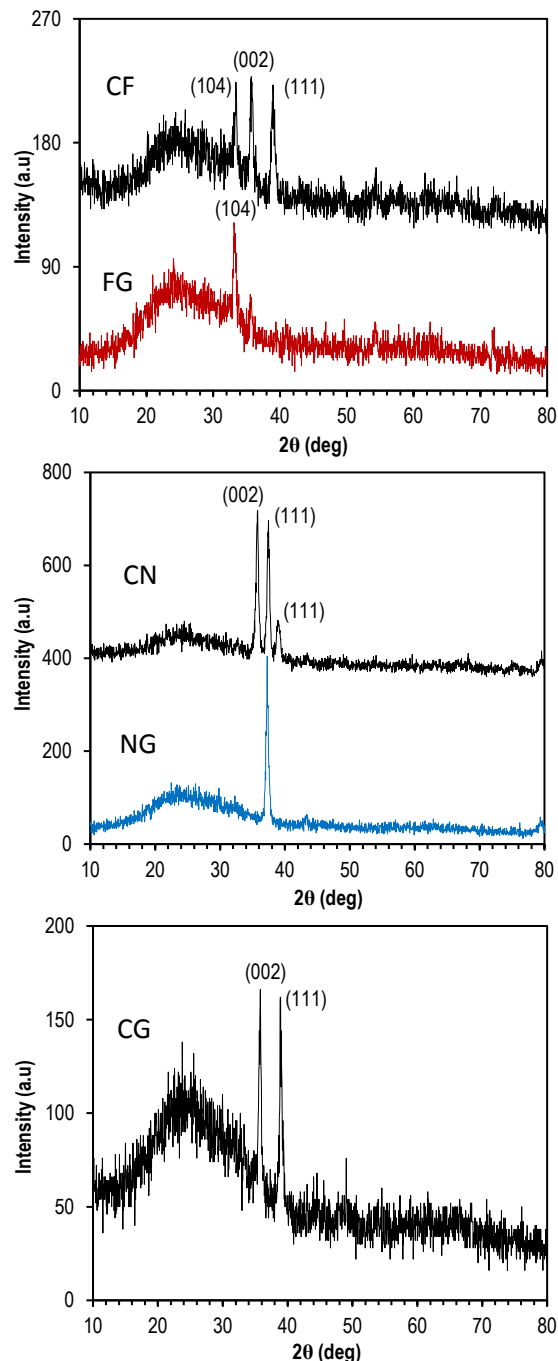
that CuO films deposited on amorphous substrate (glass) or rough seed layer results in irregular morphology with higher rate of voids among the grains while CuO deposited on relatively smoother seed layer (NG) has more regular morphology with less voids.
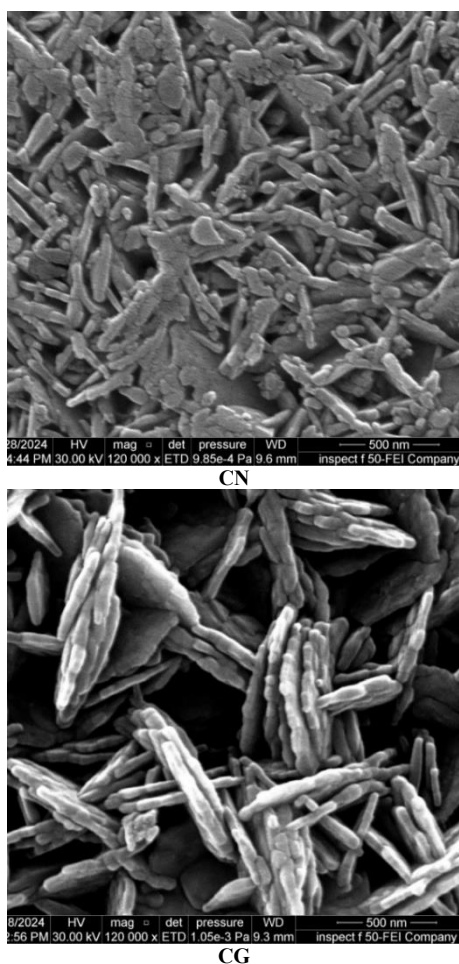

Fig. (2) XRD patterns of CuO thin films deposited by CBD technique on CuO seed layers already prepared by CSP method

Figure (3) shows FE-SEM images of the CuO thin films and their seed layers. The micrographs indicate

Fig. (3) FE-SEM micrographs for the surface of CuO thin films and NiO and Fe₂O₃ seed layers

Figure (4) reveals the cross-sectional FE-SEM image of CuO thin film on NiO seed layer. The calculation of the average lattice mismatch (LM) between CuO and three dissimilar materials namely NiO, Fe₂O₃ and Si showed that LM(CuO/NiO) = 17.15%, LM(CuO/Fe₂O₃) = 33.85%, while LM(CuO/Si) = 18.76%. This may explain why the cross-sectional imaging revealed that the CuO films deposited on NiO seed layer with minimum mismatch namely CN had the smoothest and more crystalline structure than CF. By using Image-J program, the particle size and thickness of the seed layers and the CuO thin films were estimated from the FE-SEM and presented in table (2).

It is indicated from the previous data regarding CuO thin films thickness that although the deposition process was the same, there were relatively noticeable topographic differences between CuO deposited on smoother seed layer and CuO deposited on a relatively coarse surface of Fe₂O₃ seed layer.

As shown previously in Fig. (3), the depositing CuO thin film on a relatively coarse, irregular and non-uniform seed layer yielded more porous and deformed morphology. On the other hand, glass morphology did

not prove to have coarse grains in the upcoming AFM test but the deformed morphology of CuO film deposited on it can be due to the amorphous nature of glass substrate.
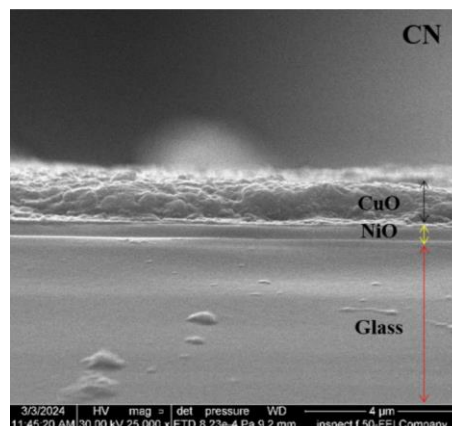

Fig. (4) Cross-sectional FE-SEM image of the CuO thin film on NiO seed layer

Table (1) Estimated values of particle size and thickness for the CuO thin films and their corresponding seed layers

Sample	Particle Size (nm)	Thickness (nm)
FG	75.04	419.89
NG	54.84	219.42
CG	52.90	870.27
CF	58.82	480.58
CN	53.10	835.72

Figure (5) shows the topography related data obtained from the AFM test. The images of AFM reveal that smoother seed layer with finer grains gives rise to a more crystallinity as indicated by more intense XRD peaks. The average roughness for NiO, Fe₂O₃ and glass substrate were estimated to be 7.58, 12.4, 0.724 nm, respectively. The root mean square values for the same samples were estimated to be 9.42, 16.7, and 0.974 nm, respectively.

Tauc's plot is widely used method to determine the value of optical bandgap energy (E_g) for semiconductors using UV-visible spectrophotometry. According to Tauc's analysis, the relationship between semiconductor the bandgap energy and the absorption coefficient for electron direct transition is given by

$$(\alpha h v)^2 = A(E_g - h v) \qquad (3)$$

Based on this equation, if we put the values of hv on the x-axis and $(\alpha h v)^2$ on the y-axis, then an extrapolation of the linear part should intersect the hv-axis at E_g. Tauc's plot is accurate method for the calculation E_g for most of the cases. However, when there is a significant reflection or scattering, discrepancies can be found between the E_g calculated from Tauc plot and the actual one. Zhong et al. [33] have introduced a technique to correct the value of E_g when there is a baseline absorption. However, there is

also another source of errors when the bandgap edge is not sharp as a result of defects or impurities. Figure (6) illustrates the difficulty facing Tauc plot method when we want to find the exact tangential line for CuO thin film on glass substrate where different tangential lines give different E_g values. To solve this problem, we propose an alternative method to find the value of bandgap energy. This method is based on drawing two tangential lines in two regions of wavelength-transmittance curve (λ-T). The tangential lines should be chosen carefully in two regions before and after a clear change in the transmittance curve-slope occurs indicating the start of absorption. After that, we find the intersection point for these two tangents. Consequently, λ_{cutoff} represents the x-axis of that intersection point. Finally, the energy gap is estimated from the cut-off wavelength using Plancks' law:

$$E_g(eV) = \frac{1240}{\lambda_{cutoff}} \qquad (4)$$

Moreover, to normalize the transmittance data with respect to the sample thickness, we divide the transmittance data by the sample thickness (t), i.e., $T_N = T/t$ then we use the normalized transmittance diagram to find the cut-off wavelength (λ_{cutoff}).
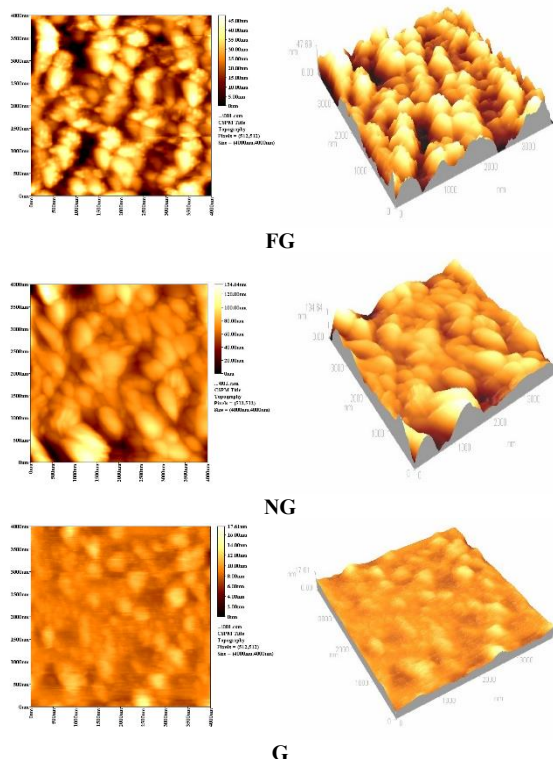

Fig. (5) 2D and 3D AFM images of NiO seed layer on glass (NG), Fe₂O₃ seed layer on glass (FG), and glass substrate (G)

Figure (7) shows the normalized transmittance versus the wavelength for the CuO thin films. The cut-off wavelength for CF, CN, and CG samples were 895, 872, and 923 nm corresponding to energy gaps 1.38,

1.42, and 1.34 eV, respectively. The obtained values by this method agree well with previous literature [34,35].
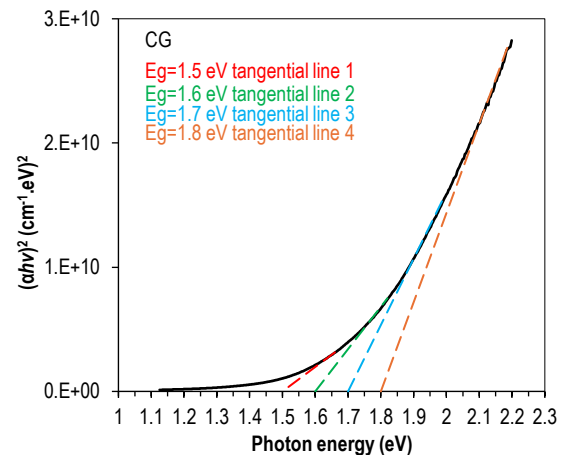

Fig. (6) Tauc plot method for finding energy band gap. More than one tangential line can be drawn leading to difficulty of determining the exact energy bandgap

The difference in the energy gap values can be correlated with the data obtained from XRD and FE-SEM results regarding varying values of the intensities of diffracted peaks that corresponds to (002) and (111) planes, particle size, and the dislocation densities. The DC conductivity of the CuO thin film was also investigated by implementing silver paint as electrodes. The conductivity (σ) was calculated from the resistivity which is given by

$$\frac{1}{\sigma}(\Omega.\,cm) = R(\Omega)\frac{A(cm^2)}{L(cm)} \qquad (4)$$

Figure (8) depicts the increase in the CuO film electrical conductivity along with the increasing in the ambient temperature.

The electrical conductivities at 30°C temperature for CF, CN, and CG samples were 2.89×10^{-5}, 2.08×10^{-5}, and 0.624×10^{-5} S/cm, respectively. These varying values can be correlated with the sum of dislocation densities obtained from XRD data, the higher values of the former resulted in higher values of electrical conductivities of the CuO films.

Hall's effect test was also implemented to determine the type of the majority charge carriers along with their density and mobility. The measurements taken from the test concluded that all CuO thin films had p-type conductivity [15] and the obtained values of previously mentioned parameters are listed in table (3).

Table (3) Hall experiment parameters for CuO thin films deposited on different seed layers

Sample	Hall's Conductivity (S/cm)	Charge's Mobility (V/ cm².s)	Charge Concentration (1/cm³)
CF	10.70E-05	8.39E-02	8.00E+15
CN	3.69E-05	4.48E-02	5.14E+15
CG	5.11E-05	2.18E-02	14.7E+15

the double heterojunction. The device C/nSi shows higher current density values which can be attributed to its higher porosity and non-uniform morphology. This type of morphology induces multiple reflections of photons that eventually they got absorbed within the depletion regions of the device resulting in higher photocurrent.
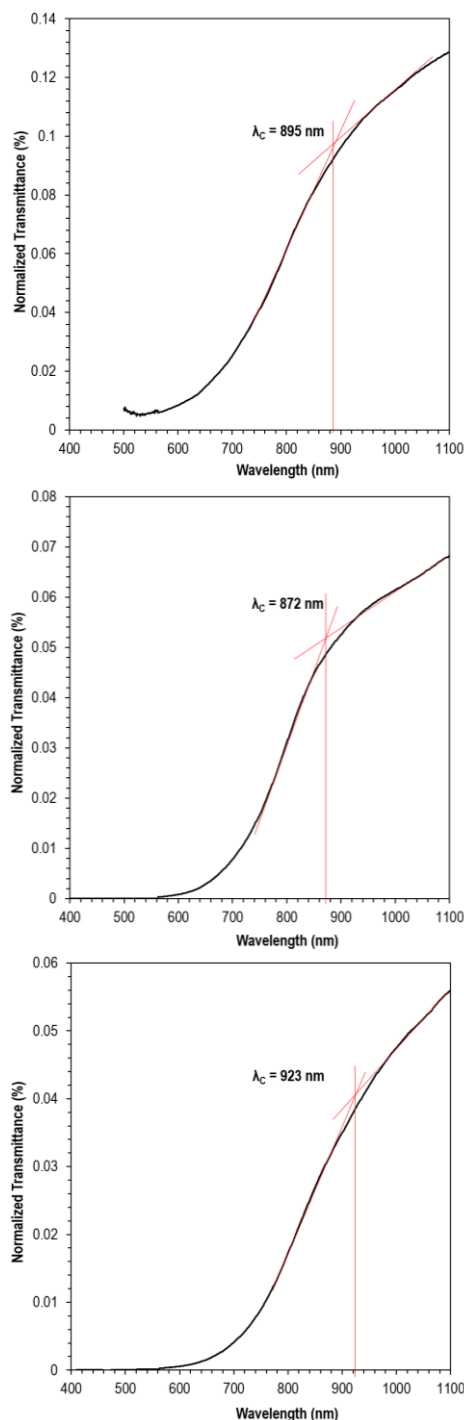

Fig. (7) Normalized transmittance versus the wavelength for CN, CF, and CG samples

Figure (9) shows the I-V characteristics of CF/nSi, CN/nSi and C/nSi heterojunctions. CF/nSi device shows relatively significant difference between the photo current and the dark current in the reverse bias which is preferable for the photodetection applications. Moreover, CN/nSi device exhibits a double heterojunction with almost symmetrical behaviour in the forward and reverse biases. Here, we assume that the existence of two depletion regions is the cause of
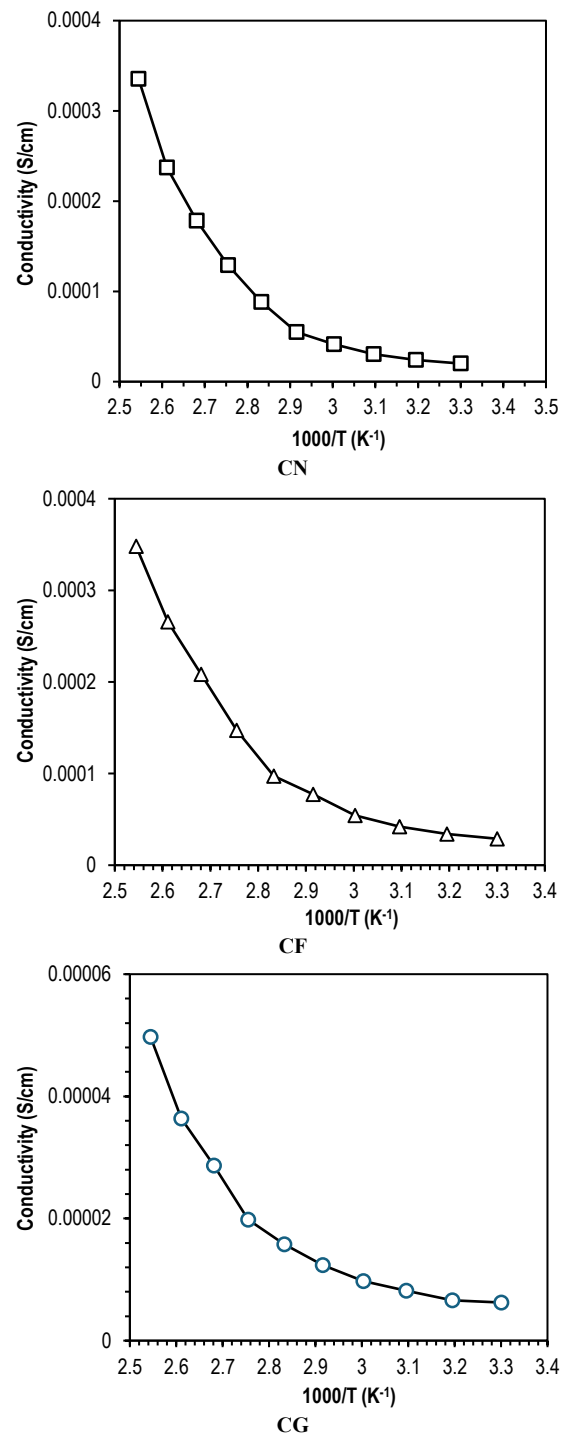

Fig. (8) Conductivity vs. reciprocal temperature for CN, CF, CG samples

Fig. (9) I-V characteristics of CN, CF, and CS (CuO on silicon) devices

The data showed improved photocurrent response of CuO thin films to white light with power density of 100 mW/cm^2. Although the difference between the photocurrent and the dark current is quite low due to high resistivity of CuO thin films prepared by CBD, but the response is promising and can be improved in the future using higher concentration of N719 dye and/or reducing the resistivity of CuO thin films using appropriate dopants.

Table (4) Improved response of CuO thin films to white light with power density of 100 mW/cm^2 after using N719 dye

Photoconductor	Dark current density (mA/cm^2)	Photocurrent density (mA/cm^2)
CF	19.12	19.5
CN	24.8	25.5
CG	17.62	17.87

4. Conclusion

CuO thin films were deposited on glass substrate, NiO, and Fe$_2$O$_3$ seed layers by chemical bath deposition method to investigate the effect of each seed layer on the properties of the CuO thin films. The results indicated that the seed layers had direct influence on the structural, optical and electrical properties of the films. CuO on more crystalline seed layers like NiO showed the lowest conductivity, and I-V characteristics indicated the formation of double heterojunctions between p-CuO/p-NiO/n-Si due to the large bandgap energy difference.

References

[1] J.C. Védrine, "Heterogeneous catalysis on metal oxides", *Catalysts*, *7*(11) (2017) 341.

[2] M.L. Grilli, "Metal oxides", *Metals*, 10(6) (2020) 820.

[3] X. Yu, T.J. Marks and A. Facchetti, "Metal oxides for optoelectronic applications", *Nature Mater.*, 15(4) (2016) 383-396.

[4] N. Yulianto et al., "Wafer-scale transfer route for top–down III-nitride nanowire LED arrays based on the femtosecond laser lift-off technique", *Microsys. Nanoeng.*, 7(1) (2021) 32.

[5] X. Wang et al., "An ultrasensitive non-enzymatic glucose sensors based on controlled petal-like CuO nanostructure", *Electrochimica Acta*, 259 (2018) 225-232.

[6] A.D. Faisal, A.A. Aljubouri and W.K. Khalef, "Photodetector fabrication based on heterojunction of CuO/SnO$_2$/Si nanostructures", *Bull. Mater. Sci.*, 45(2) (2022) 84.

[7] B. Dong, Y. Gao and J. Liu, "Preparation of SnO$_2$-SiO$_2$ film with high transmittance and strong dust-removing by sol-gel", *Optik*, 245 (2021) 167727.

[8] Q. Lv et al., "Ultrafast charge/discharge solid-state thin-film supercapacitors via regulating the microstructure of transition-metal-oxide", *J. Mater. Chem. A*, 5(6) (2017) 2759-2767.

[9] N.S. Sadeq, M.A. Hassan and Z.G. Mohammadsalih, "Preparation and study of properties of CdO: Al thin films prepared by chemical spraying", *Int. J. Thin Film Sci. Tech.*, 11(1) (2022) 101-110.

[10] W.K. Khalef, A.A. Aljubouri and A.D. Faisal, "Fabrication of Glucose biosensor electrode based on

The three samples were immersed in N719 dye solution (concentration 3×10^{-4} M) for a period of one week, then underwent photoconductivity test under specific voltage values. Table (4) lists the dark and the photocurrent densities (µA/cm^2) for CG, CF, and CN devices using 30 V dc applied voltage.

the CuO/ZnO nanostructures", in *J. Phys.: Conf. Ser.*, 1795 (2021) 012038.

[11] A.H. Mustafa, M.M. Sadeer and S.A. Duha, "Preparation Doped CuO Thin Film and Studies of Its Antibacterial Activity", *Acta Physica Polonica A*, 135(4) (2019) 596-600.

[12] M.M. Ibrahim, M.A. Hassan and K.I. Hassoon, "Novel route to prepare iron sulphide as a counter electrode for dye-sensitized solar cell", *Bull. Mater. Sci.*, 46(3) (2023) 120.

[13] M.A. Jaleel, M. A. Hassan and K.I. Hassoon, "Innovative Method to Prepare Highly Adhesive CuO Thin Films on FTO Substrates for Optoelectronic Applications", *Iraqi J. Appl. Phys.*, 19(4A) (2023) 61-66.

[14] A.K. Ali, S.E. Eli and K.I. Hassoon, "Design of high-efficiency tandem dye-sensitized solar cell with two-photoanodes toward the broader light harvesting", *Dig. J. Nanomater. Biostruct.*, 13 (2018) 299-305.

[15] M. Heinemann, B. Eifert and C. Heiliger, "Band structure and phase stability of the copper oxides Cu_2O, CuO, and Cu_4O_3", *Phys. Rev. B: Cond. Matter Mater. Phys.*, 87(11) (2013) 115111.

[16] Z.M. Sadiq, M.A. Hassan and K.I. Hassoon, "Rod-like nanostructures of copper oxide prepared by chemical bath deposition", *Eng. Technol. J.*, 40(04) (2022) 573-581.

[17] A.N. Hussain, K.I. Hassoon and M.A. Hassan, "Effect of annealing on copper oxide thin films and its application in solar cells", in *J. Phys.: Conf. Ser.*, 1530(1) (2020) 012140.

[18] Z. Wei et al., "Preparation and visible-light photocatalytic activity of α-Fe_2O_3/γ-Fe_2O_3 magnetic heterophase photocatalyst", *Mater. Lett.*, 118 (2014) 107-110.

[19] R. Bhateria and R. Singh, "A review on nanotechnological application of magnetic iron oxides for heavy metal removal", *J. Water Process Eng.*, 31 (2019) 100845.

[20] R.K. Sonker and B.C. Yadav, "Development of Fe_2O_3–PANI nanocomposite thin film-based sensor for NO_2 detection", *J. Taiwan Inst. Chem. Eng.*, 77 (2017) 276-281.

[21] A. Akbar et al., "Magnetic and magnetization properties of Co-doped Fe_2O_3 thin films", *IEEE Trans. Magnet.*, 50(8) (2014) 1-4.

[22] M. Aftab et al., "Optical and electrical properties of NiO and Cu-doped NiO thin films synthesized by spray pyrolysis", *Opt. Mater.*, 119 (2021) 111369.

[23] H.L. Chen, Y.M. Lu and W.S. Hwang, "Characterization of sputtered NiO thin films", *Surf. Coat. Technol.*, 198(1-3) (2005) 138-142.

[24] T. Ivanova et al., "Nickel oxide films deposited by sol-gel method: effect of annealing temperature on structural, optical, and electrical properties", *Materials*, 15(5) (2022) 1742.

[25] M.A. Hassan, M.H. Mohsin and R.A. Ismail, "Preparation of high-responsivity strontium–doped CuO/Si heterojunction photodetector by spray pyrolys", *J. Mater. Sci.: Mater. Electron.*, 34(10) (2023) 912.

[26] M.M. Ibrahim, M.A. Hassan and K.I. Hassoon, "Characterization of FeS_2 thin film prepared by spray pyrolysis method for optoelectronic applications", *J. Appl. Sci. Nanotech.*, 2(3) (2022) 78-84.

[27] H. Ghayour et al., "The effect of seed layer thickness on alignment and morphology of ZnO nanorods", *Vacuum*, 86(1) (2011) 101-105.

[28] J. Song and S. Lim, "Effect of seed layer on the growth of ZnO nanorods", *The J. Phys. Chem. C*, 111(2) (2007) 596-600.

[29] P. Kumar, H. No-Lee and R. Kumar, "Synthesis of phase pure iron oxide polymorphs thin films and their enhanced magnetic properties", *J. Mater. Sci.: Mater. Electron.*, 25 (2014) 4553-4561.

[30] M. Shkir et al., "An effect of Fe on physical properties of nanostructured NiO thin films for nonlinear optoelectronic applications", *Appl. Phys. A*, 126(2) (2020) 119.

[31] B.D. Cullity and S.R. Stock, **"Elements of X-ray diffraction"**, 3rd ed., Pearson Education Ltd., (Essex, 2014).

[32] K. Kapoor et al., "X-ray diffraction line profile analysis for defect study in Zr-2.5% Nb material", *Bull. Mater. Sci.*, 27 (2004) 59-67.

[33] H. Zhong et al., "Idealizing Tauc plot for accurate bandgap determination of semiconductor with ultraviolet–visible spectroscopy: a case study for cubic boron arsenide", *The J. Phys. Chem. Lett.*, 14(29) (2023) 6702-6708.

[34] J. Kampmann et al., "How photocorrosion can trick you: a detailed study on low-bandgap Li doped CuO photocathodes for solar hydrogen production", *Nanoscale*, 12 (2020) 7766–7775.

[35] Z. Wang et al., "Identifying copper vacancies and their role in the CuO based photocathode for water splitting", *Angew. Chem.*, 131 (2019) 17768–17773.

Table (2) Scherrer's analysis and dislocation density for CuO thin films, NiO and Fe_2O_3 seed layers

Sample	(hkl)	2Θ (deg)	FWHM (rad)	D(nm)	δ (1/cm²)	ε=β/4tanθ
FG	(104)	33.21	0.0083	17.45	3.29E+11	6.19 E-4
	(101)	35.64	0.0059	24.70	1.64E+11	4.74 E-4
CF	(002)	35.75	0.0092	15.89	3.98E+11	4.27E-02
	(111)	38.95	0.0123	11.97	6.98E+11	6.23E-02
NG	(111)	37.27	0.0076	19.27	2.69E+11	6.40 E-4
CN	(002)	35.75	0.0082	17.78	3.16E+11	3.60E-02
	(111)	38.95	0.0108	13.63	5.38E+11	3.99E-02
CG	(002)	35.75	0.0078	18.69	2.88E+11	1.45 E-2
	(111)	38.95	0.0079	18.63	2.86E+11	1.27 E-2